coatings

MDPI

Communication

# Synthesis of Iron Oxide Nanostructures via Carbothermal Reaction of Fe Microspheres Generated by Infrared Pulsed Laser Ablation

**Jeffrey C. De Vero [1,*,†], Alladin C. Jasmin [1,2], Lean L. Dasallas [1], Wilson O. Garcia [1] and Roland V. Sarmago [1]**

1 National Institute of Physics, University of the Philippines, Diliman, Quezon City 1101, Philippines; acjasmin@up.edu.ph (A.C.J.); ldasallas@nip.upd.edu.ph (L.L.D.); wgarcia@nip.upd.edu.ph (W.O.G.); roland.sarmago@up.edu.ph (R.V.S.)

2 Department of Physical Science, University of the Philippines, Baguio 2600, Philippines

* Correspondence: jeffrey-devero@aist.go.jp; Tel.: +81-8044338426

† Current address: National Institute of Advanced Industrial Science and Technology, Tsukuba 305-8665, Japan.

Received: 4 February 2019; Accepted: 2 March 2019; Published: 7 March 2019


**Abstract:** Iron oxide nanostructures were synthesized using the carbothermal reaction of Fe microspheres generated by infrared pulsed laser ablation. The Fe microspheres were successfully deposited on Si(100) substrates by laser ablation of the Fe metal target using Nd:YAG pulsed laser operating at $\lambda = 1064$ nm. By varying the deposition time (number of pulses), Fe microspheres can be prepared with sizes ranging from 400 nm to 10 μm. Carbothermal reaction of these microspheres at high temperatures results in the self-assembly of iron oxide nanostructures, which grow radially outward from the Fe surface. Nanoflakes appear to grow on small Fe microspheres, whereas nanowires with lengths up to 4.0 μm formed on the large Fe microspheres. Composition analyses indicate that the Fe microspheres were covered with an $Fe_3O_4$ thin layer, which converted into $Fe_2O_3$ nanowires under carbothermal reactions. The apparent radial or outward growth of $Fe_2O_3$ nanowires was attributed to the compressive stresses generated across the $Fe/Fe_3O_4/Fe_2O_3$ interfaces during the carbothermal heat treatment, which provides the chemical driving force for Fe diffusion. Based on these results, plausible thermodynamic and kinetic considerations of the driving force for the growth of $Fe_2O_3$ nanostructures were discussed.

**Keywords:** nanostructure; iron oxide; pulsed laser deposition

## 1. Introduction

Nanomaterials offer a new way of designing structural, functional, and electronic devices on the nanometer scale. These nanostructures show exceptional and dimension-dependent properties that are not readily observed in their bulk form and which can be exploited for biological and molecular applications [1–5]. In particular, $Fe_2O_3$ (iron oxide) nanostructures have been intensively studied because of their unique electrical and magnetic properties while maintaining their chemical compatibility with biological tissues for possible biological applications [1–6]. Their use extend to recording, ultrahigh density memory storage, and targeted drug delivery, including water splitting for energy applications [4–6]. Several techniques have been reported for the growth and preparation of iron oxide nanostructures, which aim at finding simple ways of controlling the morphology, size, and growth direction of these nanostructures for enhanced functionality. Most studied preparation techniques include hydrothermal synthesis [3,4], sol-gel techniques [5], thermal oxidation [6,7], electric arc gas discharge [8], and the pulsed laser deposition (PLD) method [9–11]. Common to

all these methods, metal catalysts, such as Au (template), are necessary to assist in the production of nanostructures, which partially limits the controllability of the features, size, and functionality of the nanostructures.

The PLD method offers flexibility in the growth of thin films, including the size of nanoparticles, composition, and phase, by controlling the laser excitation source (wavelength), substrate temperature, oxygen partial pressure, and target composition [12,13]. The PLD techniques have been successfully applied to prepare different oxide materials, such as superconductors [14–18], magnetic materials [19,20], perovskite cathodes, and barrier layers for solid oxide fuel cells [21–25], including perovskite thin-film solar cells [26,27]. In particular, the preparation of nanostructure thin films, such as Au-$TiO_2$ [28,29], and nanostructure multilayered perovskite cathodes [30] under different PLD growth conditions were explored. These materials in nanostructured thin film forms showed a significant enhancement of the catalytic activities as compared to their bulk counterparts. As in the case of the laser-assisted growth of one-dimensional (1D) nanostructures, such as nanowires [31,32], gas-based lasers operating in the ultraviolet wavelength (UV) were commonly utilized. However, the cost of the gas sources limits their practical application as well as the apparent deviation of the composition of the grown layer, which has a complex stoichiometry (more than three elements), thus necessitating the use of an alternative laser source for PLD assisted growth [33,34].

One possible candidate for the excitation source for PLD is the Nd:YAG laser. It is all solid-state, thus requiring no toxic and expensive gas, is easy to maintain, and is environmentally friendly. The Nd:YAG laser is also highly tunable, which can be operated from its fundamental harmonic of $\lambda$ = 1064 nm (infrared) to its fourth harmonic at $\lambda$ = 266 nm (UV). Hence, the Nd:YAG laser is a promising excitation source for a safe and low-cost PLD process. The use of the fourth harmonics ($\lambda$ = 266 nm) of the Nd:YAG for coated conductor thin film was demonstrated and showed comparable electrical properties with UV gas-based lasers [35]. Previously, we reported the use of the fundamental harmonic ($\lambda$ = 1064 nm) of the Nd:YAG laser for the preparation of high-temperature superconducting thin film materials. The initial morphology of the as-prepared samples is spheroidal, which crystallize and form a relatively smooth and flat film layer after high-temperature post-annealing (>850 °C) [36–40]. This spheroidal feature of the ablated species was observed for all types of oxide materials we investigated, suggesting that the ablated materials from the target are molten when they arrive on the substrate. Since the substrate is kept at room temperature, the ablated particles solidify on the substrate layer upon cooling. Chemical analysis of the ablated species together with time-resolved optical emission spectroscopy of the laser produced plasma during infrared pulsed laser ablation showed a strong tendency of the spheroidal particles to maintain the stoichiometry of the target [37,38]. We extended the idea of using the Nd:YAG laser operating at $\lambda$ = 1064 nm as the excitation source for the formation of nanoparticles on a Si(100) substrate coupled with the carbothermal reaction process to synthesize iron oxide nanostructures. The objective of this work is two-fold: (1) Synthesis of iron oxide nanostructures by carbothermal oxidation of Fe microspheres generated by infrared pulsed laser ablation, demonstrating the formation of iron oxide nanostructures without the need of catalysts (or self-assembly); (2) discussion of the plausible mechanism for the self-assembly of iron oxide nanostructures in terms of thermodynamics and kinetic processes.

## 2. Materials and Methods

The experiment consists of two parts: (1) Preparation of Fe microspheres by infrared ablation of Fe metal, and (2) carbothermal oxidation of Fe microspheres to generate the iron oxide nanostructures as shown in Figure 1. For the Fe microsphere preparation, a high power tunable Q-switch Nd:YAG pulsed laser (Quanta-Ray Pro Spectra Physics, Santa Clara, CA, USA) operating at the fundamental wavelength, $\lambda$ = 1064 nm, with an 8 ns pulse duration, was used to ablate a rotating Fe metal target (99.9%, Kurt J. Lesker Company, Jefferson Hills, PA, USA) with a Si(100) substrate placed 30 mm away from target as shown in Figure 1a. The ablation was performed at a laser fluence of 4.32 J/cm$^2$ at a 10 Hz repetition rate. The deposition chamber was continuously evacuated to reach a pressure of

$10^{-2}$ mbar. During the ablation process, no substrate heating and no background gas was employed. Herein, the deposition time was varied from 35 min (21,000 pulses) to 75 min (45,000 pulses) to control the density and size of nanoparticles on the Si(100) substrate. Since the substrate is kept at room temperature, the condensation of iron nanoparticles and microclusters aggregate on the Si substrate as spheroids, similar to our previous reports [37,38]. To grow the iron oxide nanowires/nanoflakes, the Fe microspheres were heat treated in a carbon-rich environment, as schematically shown in Figure 1b. Herein, the Si wafer with Fe microspheres was placed in a ceramic crucible containing 5.0 g of 99.99% activated carbon powders. The heat treatment was carried out in a box combustion furnace at temperatures between 750 to 800 °C for 145 min. To systematically evaluate the microstructural features and the composition of the Fe microspheres and $Fe_2O_3$ nanostructures, scanning electron microscopy coupled with energy dispersive x-ray spectroscopy (SEM-EDS, Hitachi S-3400N, Tokyo, Japan) was performed. Fourier transform infrared transmission spectroscopy (FTIR, Bio-Rad FTS-40A spectrometer (Cambridge, MA, USA) with KBr as the reference) was used to further confirm the iron oxide phase after thermal oxidation in the carbon-rich environment.

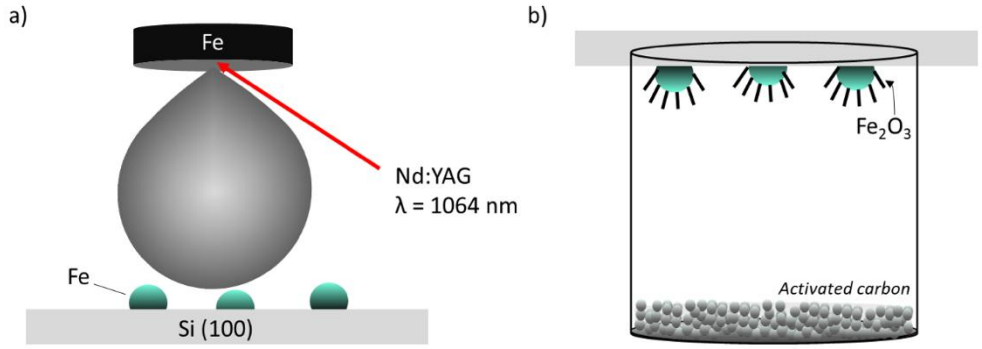


**Figure 1.** Schematic diagram of iron oxide nanostructure synthesis. The fabrication steps consist of two parts, namely (**a**) laser ablation of the Fe metal target using the Q-switch Nd:YAG pulsed laser operating at the fundamental harmonic, λ = 1064 nm. The Fe microspheres formed in the vicinity of unheated Si(100); (**b**) carbothermal oxidation of Fe microspheres at high temperatures (up to 800 °C) with activated carbon powder for 2 h. Iron oxide nanostructures grew radially outward from iron microspheres.

## 3. Results

Figure 2 shows the SEM micrographs of Fe microspheres generated by infrared laser ablation using the Nd:YAG laser. To control the size and density of the Fe microspheres, the deposition time was varied while keeping other deposition parameters fixed. Analysis of the SEM image reveals that the particle size density increases from $1.80 \times 10^3$ to $3.70 \times 10^3$ per $\mu m^2$ after fixing the deposition time to 75 min. The Fe particles are randomly distributed on the Si substrate with sizes ranging from 400 nm to 10 µm. Some Fe microspheres are smaller in size (~100 nm to 1.2 µm) at a shorter deposition time (35 min or 21,000 pulses, Figure 2a,b), whereas increasing the deposition time to 75 min (45,000 pulses) showed that large Fe microspheres up to 10 µm in diameter can be generated. At longer deposition times, the microspheres appear to coalesce together on the substrate (Figure 2c,d). The control of the microsphere density and size is possible by adjusting the laser pulses. However, the diameter of the particles has a tendency to saturate as evidenced by the distorted shape of the grains. It is possible that nanoparticles aggregated and further deposited on the microspheres as shown in Figure 2c,d. By changing the other PLD deposition conditions, such as the deposition pressure, substrate temperature, and target-to-substrate distance, it is possible to further tune the size, density, and morphological features of the grains [28,29,37]. It is interesting to note that the oxidation of the arriving particles can occur during the ablation process due to the minute amount of oxygen or during the cool down inside the growth chamber. This suggests that the Fe microspheres may have been covered with an oxide layer (oxidized) after the ablation process.

It can be seen that the characteristic feature of the surface particulates derived using infrared pulsed laser ablation is spherical or microspherical. This is because the nanoparticles, as well as the micron-sized droplets, are simultaneously generated by laser ablation. In general, to produce a thin film by PLD, the preparation condition is adjusted to decrease or suppress the droplets. More importantly, since no heat is induced on the site of arrival (usually by substrate heating), the droplets solidify, taking on a thermodynamically favored shape that in all the reported cases is spherical [36–38]. Previous studies also reveal that the ablation of a sintered target by an Nd:YAG laser operating at the infrared wavelength ($\lambda$ = 1064 nm) produces ablation species consisting of molten-like spheroidal particles with stoichiometry resembling that of the target [36–38]. Longer wavelengths result in deeper target penetration, which causes subsurface evaporation and block-by-block ejection of larger clusters, which we observed as spheroids in the substrate [12,37,38,40]. Whereas, shorter wavelengths offer a higher photon energy, which is more suitable for efficient vaporization and ionization of the solid sample, resulting in atomized material delivery on a nearby substrate [12,33]. In particular, we reported UV pulsed laser ablation of iridate targets showing iridate nanoparticles (average size ~50 nm) on unheated MgO single crystal substrates [41]. The iridate nanoparticles are spheroidal with an apparent tendency to increase its particle density with increasing laser fluence [40]. The formation of large ZnO microspheres (sizes of more than 30 μm) was successfully synthesized using very high laser fluences up to 440 J/cm$^2$ (which is $10^3$ higher than conventional laser density used in PLD) [41]. However, undesired severe target fragmentation was observed at this range of laser fluence. The systematic variation of the deposition conditions to create different features of iron microstructures is out of the scope of this work and is suggested for future studies.

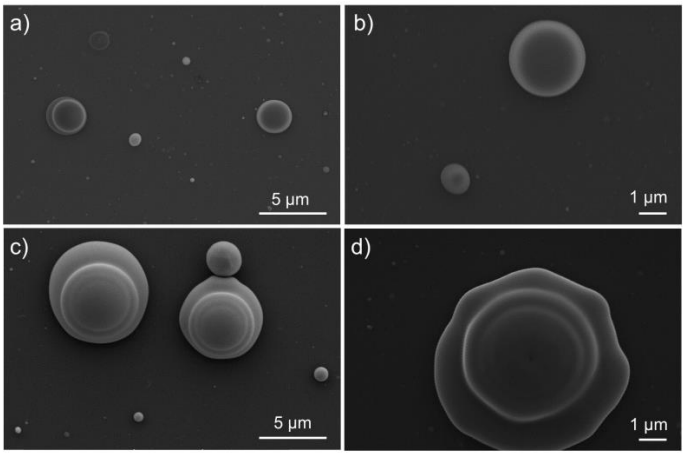


**Figure 2.** Fe microspheres on Si(100) generated by infrared pulsed laser ablation at deposition time of (**a**,**b**) 35 min (21,000 pulses); (**c**,**d**) 75 min (45,000 pulses). The surface features of Fe grains suggests that they are molten and cool when they arrive on the substrate.

Figure 3 shows the Fe microspheres ($D$ = 10 μm) after carbothermal heat treatment at (a,b) 750 °C and (c,b) 800 °C for 145 min. It can be observed that iron oxide nanostructures grew radially outward from the surface of Fe microspheres. At 750 °C, iron oxide nanowires grew outward from the surface of Fe microspheres. The iron oxide nanostructures' diameters, $D$, vary from 500 nm (nanoflakes) to 2 μm (nanowires) as shown in Figure 3a. Nanosize pores on the surface of Fe microspheres are also evident at 750 °C (Figure 3a,b). On the other hand, carbothermal treatment at 800 °C decreases the size of the Fe microspheres, but results in longer nanowires extending up to $L$ = 4.0 μm with a large aspect ratio ($L/D$ = 44) as shown in Figure 3c. This suggests that increasing the carbothermal temperature assists in the growth of iron oxide nanowires. Pores are also present on the surface as well as some nanoflakes growing adjacent to the nanowires as shown in Figure 3d. A representative SEM micrograph of small microspheres ($D$ = 1.8 μm) prepared at shorter laser pulses is also shown for comparison (Figure 3e). Nanoflakes appear to dominate the surface with no apparent growth

of nanowires. The difference in the morphology of the iron oxide nanostructure indicates that the growth of nanowires sensitively changes with the size of the Fe microspheres. This suggests that large (>10.0 μm) microspheres are necessary to provide a sufficient supply of Fe during the carbothermal process for the growth of iron oxide nanowires. To illustrate the role of the carbon-rich environment in the self-assembly of iron oxide nanostructures, a reference Fe microsphere was oxidized in air (or without carbon) as shown in Figure 3f. It is clear from this result that the oxidation in air (or the trace amount of $CO_2$ in air) is insufficient to generate iron oxide nanowires, indicating that high vapor pressure carbon (or high density of carbon gaseous species) is critical for the synthesis of iron oxide nanostructures. The mechanistic growth of iron oxides under the carbothermal route will be discussed later. It is interesting to note that by changing the size/temperature, the resulting dimensions of the nanowires can be tuned, suggesting a flexibility of the infrared pulsed laser ablation assisted carbothermal growth of nanostructures. As the diameter of the wire decreases, the number of surfaces greatly increases. Hence, the large surface-to-volume ratio of the nanowire is expected to increase the number of active surfaces, which alters the physiochemical properties of the nanowires. A large aspect ratio is highly ideal for improving the sensitivity of the nanowires for real-time monitoring for sensor applications [1–7]. As a prospective future work, the micromanipulation and harvesting of iron oxide nanowires using the cantilevers of an atomic force microscope should be performed to isolate iron oxide nanowires for possible electronic applications (which our group has successfully demonstrated in the case of hydrothermally prepared ZnO nanowires exhibiting highly suitable scintillation properties, see [42,43]).

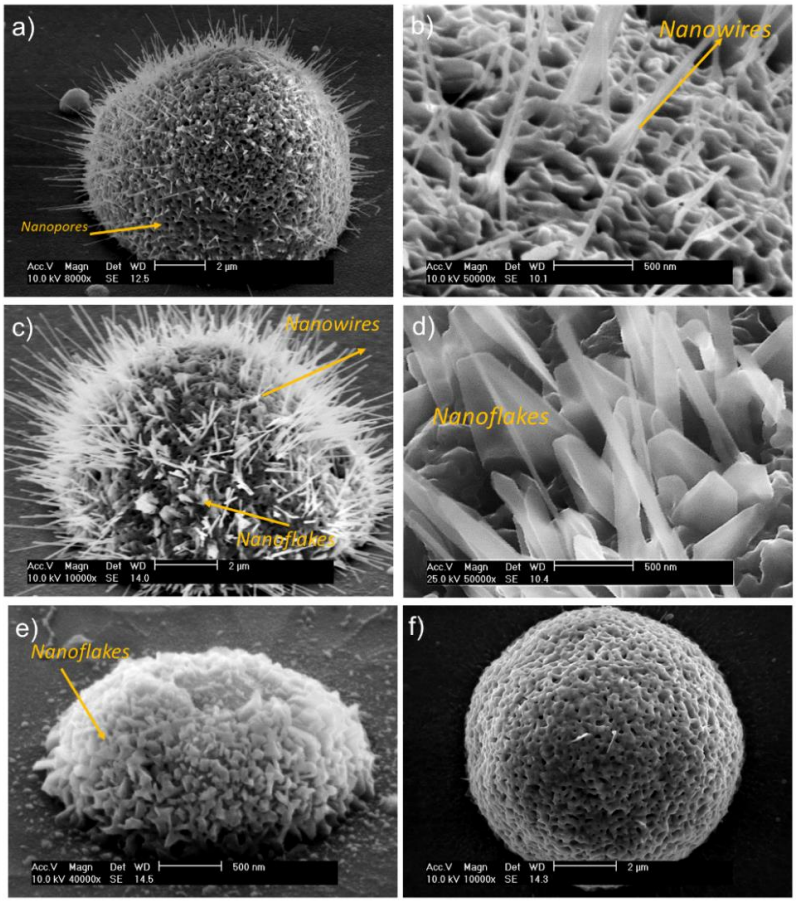


**Figure 3.** Fe microspheres (average diameter, $D$ = 10 μm) after carbothermal heat treatment at (**a**,**b**) 750 °C and (**c**,**d**) 800 °C. The size and features of the iron oxide nanostructure sensitively change with temperature; (**e**) limited growth of nanoflakes on smaller Fe microspheres ($D$ = 1.8 μm diameter); (**f**) reference Fe microsphere heat-treated in air.

Figure 4a shows the cross-sectional SEM image of iron oxide nanowires radially growing from the surface of Fe microspheres, which can extend up to 10 μm in length. The nanowires have a sharp tip with well-defined edges (290 nm in length) as shown in Figure 4b. The diameter of the iron oxide nanowires is typically around 440 nm. To elucidate the phase of the iron oxide nanowire generated by infrared pulsed laser ablation with the carbothermal technique, representative FTIR transmittance spectroscopy was performed as shown in Figure 4c. The FTIR spectra show absorbance peaks at 457.0 and 667.0 $cm^{-1}$ as indicated in the figure. The characteristic absorption bands of the $Fe_2O_3$ phase are at 460 $cm^{-1}$ (transverse-optical mode, TO) and 537 $cm^{-1}$ (longitudinal-optical mode, LO). The FTIR spectra of the iron oxide nanostructure showed a small phase shift (3.0 $cm^{-1}$) in the TO mode and (5.0 $cm^{-1}$) LO mode as compared to the reported values of the TO and LO for $Fe_2O_3$ [44,45]. Representative EDS spectrum with a semi-quantitative analysis of Fe and O of the iron oxide nanostructure is shown in Figure 4d. The EDS confirmed that the nanowires contain both Fe and O in approximately a 2:3 ratio, indicating the formation of $Fe_2O_3$, which is consistent with the FTIR results. Hence, the iron oxide nanostructure formed can be assigned to the $Fe_2O_3$ phase. A trace amount of C was detected from the carbon used in the coating of the sample. Si was also detected since EDS may include some information from the substrate because of the penetration of the electron beam.

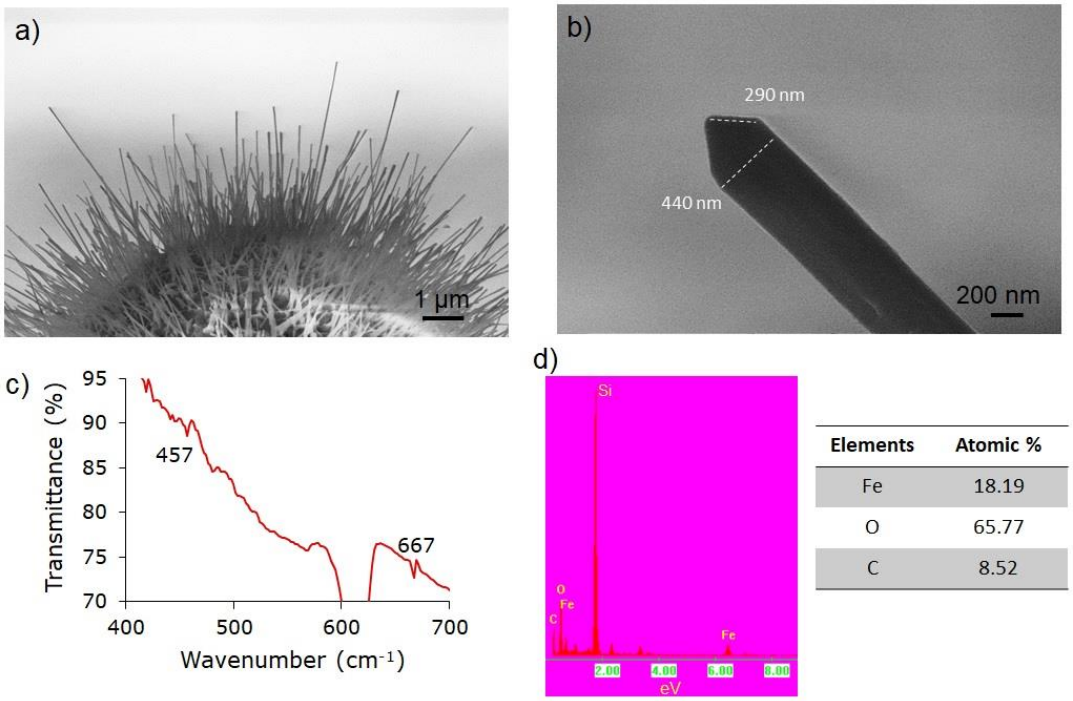


| Elements | Atomic % |
|---|---|
| Fe | 18.19 |
| O | 65.77 |
| C | 8.52 |

**Figure 4.** (**a**) SEM cross-sectional image of iron oxide nanostructures after carbothermal heat treatment showing the formation of iron oxide growing radially outward from the surface of Fe microspheres. (**b**) Representative high-resolution image of an iron oxide nanowire with well-defined edges. (**c**) FTIR spectra, (**d**) EDS spectra, and semi-quantitative analysis of the iron oxide nanostructures confirming the formation of the $Fe_2O_3$ phase.

## 4. Discussion

To describe the plausible growth mechanism of $Fe_2O_3$ nanostructures under the carbothermal reaction, the following chemical reactions are considered. The reaction of carbon and Fe with oxygen in air proceeds as follows:

$$C\ (s) + O_2\ (g) \rightarrow CO_2\ (g) \quad (1)$$

whereas:

$$3\ Fe\ (s) + 2\ O_2\ (g) \rightarrow Fe_3O_4 \quad (2)$$

Based on our results, the $Fe_3O_4$ appears to be in the intermediate phase of the nanoparticles or may be present in the walls of the microspheres and may react with carbon dioxide, forming $Fe_2O_3$ in the process:

$$2\ Fe_3O_4\ (s) + CO_2\ (g) = 3\ Fe_2O_3 + CO\ (g) \quad (3)$$

Alternatively, $Fe_3O_4$ may react with CO (g) following the reduction process:

$$Fe_3O_4\ (s) + CO\ (g) = 3\ FeO\ (s) + CO_2\ (g) \quad (4)$$

$$FeO\ (s) + CO\ (g) = Fe\ (s) + CO_2\ (g) \quad (5)$$

Note that gasification of solid carbon can also occur under large amounts of $CO_2$ gas via [46]:

$$C(s) + CO_2\ (g) = 2CO\ (g) \quad (6)$$

Hence, it possible that Equations (3) and (4) may occur simultaneously. The cycle proceeds until a sufficient supply of Fe is available to form $Fe_2O_3$ nanostructures, which in this case can be inferred from the change of the highly smooth surface of Fe microspheres to a rough porous like surface after the carbothermal reaction. In the case of the two stable oxide phases of $Fe_3O_4$ and $Fe_2O_3$, we can hypothesize that the surface contains two layers. The $Fe_2O_3$ may form at the outmost layer and subsurface of the less oxidized oxide phase containing $Fe_3O_4$. The ratio of these phases depends on the availability of Fe species present in bulk. It is highly improbable that Fe and C affect the $Fe_3O_4$-$Fe_2O_3$ layer and the reduction of $Fe_3O_4$ at the surface once both phases are established during the reaction. These reaction steps suggest that both supplies of Fe and carbon species are critically important to producing the $Fe_2O_3$ nanostructures. In other words, the availability of both Fe and C are the rate-limiting steps. In the absence of a sufficient carbon supply (low carbon vapor pressure), $Fe_3O_4$ may form around the walls of iron microspheres, which is consistent with our observation (Figure 3e) [47], and ceases to be converted to $Fe_2O_3$. Previously, we reported the spectroscopic analysis of the Fe layer on Si(100) carbothermally heat treated at 800 °C [47]. Raman spectroscopy reveals that the iron oxide nanostructures after carbothermal heat treatment were predominantly the $Fe_2O_3$ phase. A significantly broad $Fe_3O_4$ peak was also detected with respect to the literature value [48], suggesting that remnant $Fe_3O_4$ may be present in the sample, which did not fully convert to the $Fe_2O_3$ phase. The large shift in the observed $Fe_3O_4$ peak suggests that the $Fe_3O_4$ layer is less crystalline and more strained on the Fe microsphere than the highly faceted $Fe_2O_3$ nanowires. Based on the SEM analysis, the initially smooth surface of the Fe microspheres transformed into a rough and porous-like structure, which is a characteristic feature of the $Fe_3O_4$ film after thermal oxidation [46]. We take this to indicate that the walls of Fe microspheres contain a thin layer of $Fe_3O_4$. Kinetically, the solid–solid reaction is expected to be much slower compared to gas–solid. Hence, the driving force for $Fe_2O_3$ formation is the availability of carbon gas species surrounding the iron oxide nanoparticles [49].

To plausibly describe the apparent radial or outward growth of $Fe_2O_3$ nanowires on the surface of Fe microspheres generated by infrared pulsed laser ablation, we propose that compressive stresses are generated across the iron oxide interfaces during carbothermal processes, leading to the formation of iron nanostructures, as schematically shown in Figure 5. The atomic flux can be described using Fick's second law of diffusion [50] via:

$$J = cB\ \Delta\mu \quad (7)$$

where $c$ is the concentration of the diffusion species (Fe), $B$ is the mobility, and $\Delta\mu$ is the chemical potential gradient. The chemical potential gradient can be expressed in terms of the gradient of the hydrostatic pressure [51], σ, and can serve as the driving force, which can be written as:

$$J = \frac{cDV}{k_B T}\ \Delta\sigma \quad (8)$$

where the mobility, $B$, can be expressed as a factor of the diffusion coefficient, $D$, and the atomic ($V$) volume per unit of Boltzmann's constant, $k_B$, and the absolute temperature, $T$. The atomic flux is then directed from a more compressive/less tensile area to a less compressive/more tensile area. When Fe spheroids are heated in a carbon-rich environment, as described in the chemical reactions above, two thermodynamically stable oxide layers are formed, namely, $Fe_3O_4$ to $Fe_2O_3$ [49]. Since the molar volumes were in the order of Fe, or FeO < $Fe_3O_4$ < $Fe_2O_3$, hydrostatic stresses are generated across the interface. In this process of formation, Fe ions migrate from the Fe microsphere to the surface via bulk diffusion, leaving pores in the process. Fe ions can reach the $Fe_3O_4/Fe_2O_3$ via grain boundary diffusion. The $Fe_3O_4$ maybe in the transient state, transforming into $Fe_2O_3$ in the presence of a carbon-rich environment. The fast migration of Fe via surface diffusion can further promote the length of $Fe_2O_3$ nanowires. Hence, the migration of Fe ions via different diffusion pathways across the surface provides a continuous supply for the growth of the $Fe_2O_3$ nanowires. In this sense, larger sizes of Fe microspheres provide a larger volume for the mass transport of Fe ions. Large Fe microspheres (>10.0 μm) generate nanowires whereas small Fe microsphere result in the formation of nanoflakes. Our result is similar to the growth of CuO nanowires by hydrostatic stresses induced by the formation of different molar species of Cu across the Cu/Si interface under heat treatment [51]. The driving force for the growth of CuO nanowires was attributed to the stresses induced in the samples during annealing in air. Cu flux, which tends to migrate to some specific sites through surface and grain boundaries, provides for the growth of CuO nanowires [51]. The stress gradient determines the direction of $Fe_2O_3$.

The sufficient presence of $CO_2$ during heat treatment (or a carbon rich-environment) allows for the simultaneous reaction and reduction of Fe species, which is essential for the self-assembly of $Fe_2O_3$ nanostructures. Oxidation in air of the Fe microsphere did not produce an $Fe_2O_3$ nanostructure, indicating that the supply of both Fe and carbon are the rate-limiting steps for the growth of $Fe_2O_3$ nanostructures. Various stages of the growth formation of iron oxide nanostructures are schematically shown in Figure 5. Herein, Fe may diffuse from the bulk (microsphere) to the surface and may react with the oxygen and or carbon forming intermediate phase, $Fe_3O_4$ (stage 1 to stage 2). Fe ions may further diffuse at the $Fe_3O_4/Fe_2O_3$ interface via the grain boundary, whereas Fe may be transported through the nanowires via surface diffusion (stage 3). The diffusion of Fe ions through the nanowires was also reported to occur during the thermal oxidation of Fe metal at 600 °C, resulting in the growth of $Fe_2O_3$ nanowires [52], which is consistent with our results. In fact, the diffusivity of Fe ions is enhanced at high-temperatures (as in our case, which is 800 °C). Hence, the length of iron oxide nanowires strongly depends on the diffusion of Fe through the iron oxide interface. However, for growth to proceed, a carbon-rich environment is necessary as described in the chemical reactions presented in Equations (3)–(5). This is an important consideration in controlling the type of iron oxide nanostructure. Another possible growth route is via diffusion assisted seed crystal growth, however, the evidence suggests the contrary. As shown in Figure 3f, although Fe (seed) is present, the Fe/air interface did not produce iron oxide nanowires. However, under the carbothermal reaction route, the self-assembly of iron oxide nanowires occurred. The size and length of these nanowires are kinetically and thermodynamically controlled by the diffusion of Fe and the availability of carbon in air. It is important to note that in most surface-diffusion induced growth of nanowires, such as ZnO, the nanowires are prepared with small Au clusters on GaN substrates [53,54] and/or in Zn acetate seeds on amorphous substrates, where the diffusion of Zn ions controls the length of the nanowires [55]. A thorough discussion on the growth of ZnO nanowires from Zn-based seeds can be found in [55]. However, iron oxide nanowires were observed to grow on the surface of microspheres even without a catalyst as long as a sufficient amount of carbon was present, which was supplied by heating the activated carbon at high temperatures. The influence of the strain in the iron oxide nanostructure may also be explored in future works by changing the type of oxide substrate.

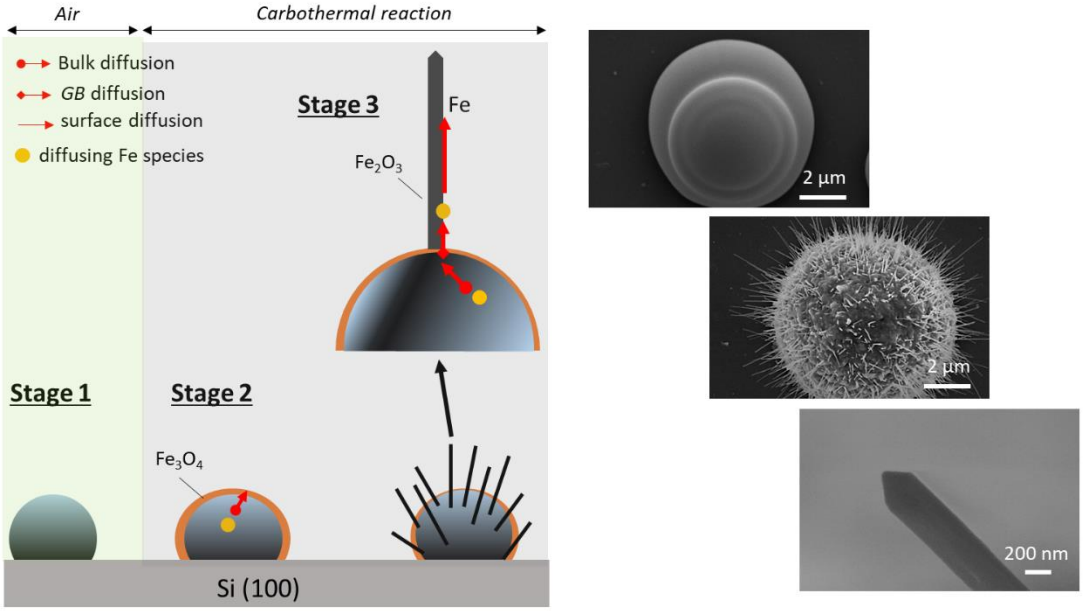


**Figure 5.** Plausible growth process of $Fe_2O_3$ nanowires under the carbothermal route. Key stages can be identified: Stage 1, deposition of the Fe microsphere; Stage 2, initial stage of the carbothermal annealing of Fe microspheres transform into $Fe_3O_4$ as the intermediate phase; Stage 3: final stage of carbothermal annealing, with the $Fe_3O_4$ transforming mostly into $Fe_2O_3$ nanowires. The stress gradient determines the direction of $Fe_2O_3$. Nanowires emerge from the $Fe/Fe_3O_4$ interface to outward stress-free $Fe_2O_3$ nanowire. Different types of pathways, such as bulk, grain boundary (GB), and surface diffusion, can assist in the transport of Fe across the interfaces. Representative SEM images of the Fe microsphere generated by infrared pulsed laser ablation and the carbothermally synthesized iron oxide nanostructures are also shown in the figure.

## 5. Summary

In summary, the formation of iron oxide nanostructures was successfully demonstrated using combined infrared pulsed laser ablation and carbothermal heat treatment of Fe microspheres. Results show that iron oxide nanowires and nanoflakes can be synthesized without the need of a catalyst. The iron oxide nanostructures grew radially outward from the Fe microspheres, suggesting a possible growth via self-assembly. Chemical and morphological analyses indicate that the synthesized iron oxide nanostructures can be attributed to the $Fe_2O_3$ phase. The plausible growth mechanism of iron oxide nanowires was described in terms of the chemical driving force for the diffusion of Fe species through the microsphere, as well as $Fe_3O_4/Fe_2O_3$ interfaces, which are both thermodynamically and kinetically controlled by the amounts of Fe and carbon gaseous species. The features of the nanoparticles can be easily tuned by simply adjusting the number of laser pulses or depositions during infrared pulsed laser ablation. The features of the iron oxide nanostructure (nanoflakes or nanowires) appeared to strongly depend on the size of the Fe microspheres. We also demonstrated that a sufficient amount of carbon during the heat treatment of Fe microspheres is necessary to generate iron oxide nanowires. An investigation of the electrical and magnetic properties of $Fe_2O_3$ is recommended for future work. It is interesting to note that the iron oxide nanostructures from infrared pulsed laser ablation result in the growth of $Fe_2O_3$ nanowires with a high aspect ratio. Iron oxide nanostructures with a high aspect ratio are highly suitable for bioengineering applications. Hence, this method is highly advantageous in fabricating iron oxide nanostructures with a high aspect ratio. It is important to point out that the use of an all solid-state laser, such as the Nd:YAG pulsed laser, allows for the controllable synthesis of nanostructure materials. It is envisioned that infrared laser ablation in combination with carbothermal heat-treatment could be a viable method to grow other nanostructured functional materials.

**Author Contributions:** Conceptualization, J.C.D.V. and A.C.J.; Methodology, J.C.D.V., A.C.J., L.L.D. and W.O.G.; Investigation, J.C.D.V. and A.C.J.; Data curation, J.C.D.V. and A.C.J.; Writing, J.C.D.V. and A.C.J.; Visualization, J.C.D.V. and A.C.J.; Supervision, R.V.S.; Funding acquisition, R.V.S.

**Funding:** This research received no external funding.

**Acknowledgments:** A. Jasmin acknowledges UP Baguio Local Faculty Fellowship Grant. University of the Philippines assisted in meeting the publication costs of this article.

**Conflicts of Interest:** The authors declare no conflict of interest.

## References

1. Bery, C. Progress in functionalization of magnetic nanoparticles for applications in biomedicine. *J. Phys. D Appl. Phys.* **2009**, *42*, 224003. [CrossRef]
2. Xie, Y.; Ju, Y.; Toku, Y.; Morita, Y. Synthesis of single-crystal $Fe_2O_3$ nanowire array based on stress-induced atomic diffusion used for solar water splitting. *R. Soc. Open Sci.* **2018**, *5*, 171226. [CrossRef]
3. Takami, S.; Sato, T.; Mousava, T.; Ohara, S.; Umetsu, M.; Adschiri, T. Hydrothermal synthesis of surface-modified iron oxide nanoparticles. *Mater. Lett.* **2007**, *61*, 4769–4772. [CrossRef]
4. Li, J.; Shi, X.X.; Shen, M. Hydrothermal synthesis and functionalization of iron oxide nanoparticles for MR imaging applications. *Part. Part. Syst. Charact.* **2014**, *31*, 1223–1237. [CrossRef]
5. Walker, J.; Tannenbaum, R. Characterization of the sol−gel formation of iron (III) oxide/hydroxide nanonetworks from weak base molecule. *Chem. Mater.* **2006**, *18*, 4793–4801. [CrossRef]
6. Hiralal, P.; Unalan, H.; Wijayantha, K.; Kursumovic, A.; Jefferson, D.; MacManus-Driscoll, J.; Amaratunga, G. Growth and process conditions of aligned and patternable films of iron(III) oxide nanowires by thermal oxidation of iron. *Nanotechnology* **2008**, *19*, 455608. [CrossRef] [PubMed]
7. Yu, W.; Falker, J.; Yavuz, C.; Colvin, V. Synthesis of monodisperse iron oxide nanocrystals by thermal decomposition of iron carboxylate salts. *Chem. Commun.* **2004**, 2306–2307. [CrossRef] [PubMed]
8. Xue, D.; Gao, C.; Liu, Q.; Zhang, L. Preparation and characterization of hematite nanowire arrays. *J. Phys. Condens. Matter* **2003**, *15*, 1455. [CrossRef]
9. Shi, W.; Zheng, Y.; Peng, H.; Wang, N.; Lee, C.S.; Lee, S.T. Laser ablation synthesis and optical characterization of silicon carbide nanowires. *J. Am. Ceram. Soc.* **2000**, *83*, 3228–3330. [CrossRef]
10. Yu, D.; Sun, X.; Lee, C.; Bello, I.; Lee, S.; Gu, H.; Leung, K.; Zhou, G.; Dong, Z.; Zhang, Z. Synthesis of boron nitride nanotubes by means of excimer laser ablation at high temperature. *Appl. Phys. Lett.* **1998**, *72*, 1966–1967. [CrossRef]
11. Wang, N.; Zhang, Y.F.; Tang, Y.H.; Lee, C.S.; Lee, S.T. $SiO_2$-enhanced synthesis of Si nanowires by laser ablation. *Appl. Phys. Lett.* **1998**, *73*, 3902–3904. [CrossRef]
12. Chrisey, D.B. *Pulsed Laser Deposition of Thin Films*; Wiley-Interscience: New York, NY, USA, 1994; ISBN 978-0471592181.
13. Eason, R. *Pulsed Laser Deposition of Thin Films Applications-Led Growth of Functional Materials*; Wiley-Interscience: New York, NY, USA, 2006; ISBN 978-0471447092.
14. Dijkkamp, D.; Venkatesan, T.; Wu, X.D.; Shaheen, S.A.; Jiswari, N.; Min-lee, Y.H.; McLean, W.L.; Croft, M. Preparation of Y-Ba-Cu oxide superconductor thin films using pulsed laser evaporation from high $T_c$ bulk material. *Appl. Phys. Lett.* **1987**, *51*, 619–621. [CrossRef]
15. de Vero, J.; Lee, D.; Shin, H.; Namuco, S.; Hwang, I.; Sarmago, R.; Song, J.H. Influence of deposition conditions on the growth of micron-thick highly *c*-axis textured superconducting $GdBa_2Cu_3O_{7-\delta}$ films on $SrTiO_3$ (100). *J. Vac. Sci. Technol.* **2018**, *36*, 031506. [CrossRef]
16. de Vero, J.; Hwang, I.; Santiago, A.; Chang, J.; Kim, J.; Sarmago, R.; Song, J. Growth of $Bi_2Sr_2CaCu_2O_{8+\delta}$ thin films with enhanced superconducting properties by incorporating $CaIrO_3$ nanoparticles. *Appl. Phys. Lett.* **2014**, *104*, 172603. [CrossRef]
17. Wu, X.D.; Dye, R.C.; Muenchausen, R.E.; Foltyn, S.R.; Maley, M.; Rollett, A.D.; Garcia, A.R.; Nogar, N.S. Epitaxial $CeO_2$ films as buffer layers for high-temperature superconducting thin films. *Appl. Phys. Lett.* **1991**, *58*, 2165. [CrossRef]
18. Singh, R.; Kumar, D. Pulsed laser deposition and characterization of high-$T_c$ $YBa_2Cu_3O_{7-x}$ superconducting thin films. *Mater. Sci. Eng. Rep.* **1998**, *22*, 113–185. [CrossRef]

19. Shen, J.; Gai, Z.; Kirschner, J. Growth and magnetism of metallic films and multilayers by pulsed laser deposition. *Surf. Sci. Rep.* **2004**, *52*, 163–218. [CrossRef]
20. Chen, X.; Chien, C. Magnetic properties of epitaxial Mn-doped ZnO thin films. *J. Appl. Phys.* **2003**, *93*, 7876–7878. [CrossRef]
21. Plonczak, P.; Søgaard, A.B.M.; Ryll, T.; Martynczuk, J.; Hendriksen, P.; Gauckler, L. Tailoring of $La_xSr_xCo_yFe_{1-y}O_{3-\delta}$ nanostructure by Pulsed Laser Deposition. *Adv. Funct. Mater.* **2011**, *21*, 2764–2775. [CrossRef]
22. de Vero, J.C.; Develos-Bagarinao, K.; Kishimoto, H.; Ishiyama, T.; Yamaji, K.; Horita, T.; Yokokawa, H. Enhanced stability of solid oxide fuel cells by employing a modified cathode- interlayer interface with a dense $La0_{.6}Sr_{0.4}Co_{0.2}Fe_{0.8}O_{3-\delta}$ thin film. *J. Power Sources* **2018**, *377*, 128–135. [CrossRef]
23. de Vero, J.C.; Develos-Bagarinao, K.; Kishimoto, H.; Ishiyama, T.; Yamaji, K.; Horita, T.; Yokokawa, H. Optimization of GDC interlayer against $SrZrO_3$ formation in LSCF/GDC/YSZ triplets. In Proceedings of the 12th European SOFC and SOEC Forum, Lucerne, Switzerland, 5–8 July 2016; Volume 41, p. B1513.
24. Morales, M.; Pesce, A.; Slodczyk, A.; Torrell, M.; Piccardo, P., II; Montinaro, D.; Tarancón, A.; Morata, A. Enhanced performance of gadolinia-doped ceria diffusion barrier layers fabricated by pulsed laser deposition for large-area solid oxide fuel cells. *ACS Appl. Energy Mater.* **2018**, *1*, 1955–1964. [CrossRef]
25. Yan, J.; Matsumoto, H.; Akbay, T.; Yamada, T.; Ishihara, T. Preparation of $LaGaO_3$-based perovskite oxide film by pulsed-laser ablation method and application as a solid oxide fuel cell electrolyte. *J. Power Sources* **2006**, *157*, 714–719. [CrossRef]
26. Liang, Y.; Yao, Y.; Zhang, X.; Hsu, W.; Gong, Y.; Shin, J.; Wachsman, E.; Dagenais, M.; Takeuchi, I. Fabrication of organic-inorganic perovskite thin films for planar solar cells via pulsed laser deposition. *AIP Adv.* **2016**, *6*, 05001. [CrossRef]
27. Park, J.; Seo, J.; Park, S.; Shin, S.; Kim, Y.; Jeon, N.; Shin, H.; Noh, T.A.J.; Yoon, S.; Hwang, C.; et al. Efficient $CH_3NH_3PbI_3$ perovskite solar cells employing nanostructured p-Type NiO electrode formed by a pulsed laser deposition. *Adv. Mater.* **2015**, *27*, 4013–4019. [CrossRef] [PubMed]
28. Ghidelli, M.; Mascaretti, L.; Bricchi, B.; Zapelli, A.; Russo, V.; Casari, C.; Bassi, A.L. Engineering plasmonic nanostructured surfaces by pulsed laser deposition. *Appl. Surf. Sci.* **2018**, *433*, 1064–1073. [CrossRef]
29. Bricchi, B.; Ghidelli, M.; Mascaretti, L.; Zapelli, A.; Russo, V.; Casari, C.; Terraneo, G.; Alessandri, I.; Ducati, C.; Bassi, A.L. Intergration of plasmonic Au nanoparticles in $TiO_2$ hierarichal structures in a single-step pulsed laser co-deposition. *Mater. Des.* **2018**, *156*, 311–319. [CrossRef]
30. Develos-Bagarinao, K.; de Vero, J.; Kishimoto, H.; Yamaji, K.; Horita, T.; Yokokawa, H. Multilayered LSC and GDC: An approach for designing cathode materials with superior oxygen exchange properties for solid oxide fuel cells. *Nano Energy* **2018**, *52*, 369–380. [CrossRef]
31. Yang, R. One-Dimensional Nanostructures by Pulsed Laser Ablation. *Sci. Adv. Mater.* **2012**, *4*, 401–406. [CrossRef]
32. Morales, A.; Lieber, C. A laser ablation method for synthesis of crystalline semiconductor nanowires. *Science* **1998**, *279*, 208–211. [CrossRef] [PubMed]
33. Schou, J. Physical aspects of the pulsed laser deposition technique: The stoichiometric transfer of material from target to film. *Appl. Surf. Sci.* **2009**, *10*, 5191–5198. [CrossRef]
34. Arnold, C.B.; Aziz, M.J. Stoichiometry issues in pulsed laser deposition of alloys grown from multicomponent targets. *Appl. Phys. A* **1999**, *69*, S23–S27. [CrossRef]
35. Ichino, Y.; Yoshida, Y.; Yoshimura, T.; Takai, Y.; Yoshizumi, M.; Izumi, T.; Shiohara, Y. Potential of Nd:YAG pulsed laser deposition method for coated conductor production. *Phys. C* **2010**, *470*, 1234–1237. [CrossRef]
36. de Vero, J.; Blanca, G.R.S.; Vitug, J.; Garcia, W.; Sarmago, R. Stoichiometric transfer of material in the infrared pulsed laser deposition of yttrium doped Bi-2212 films. *Phys. C* **2011**, *471*, 378–383. [CrossRef]
37. de Vero, J.; Gabayno, J.F.; Garcia, W.O.; Sarmago, R.V. Growth of $Bi_2Sr_2CaCu_2O_{8+\delta}$ thin films deposited by infrared (1064 nm) pulsed laser deposition. *Phys. C* **2010**, *470*, 149–154. [CrossRef]
38. Vitug, J.; de Vero, J.; Blanca, G.R.S.; Sarmago, R.; Garcia, W. Stoichiometric transfer by infrared pulsed laser deposition of y-doped Bi–Sr–Ca–Cu–O investigated using time-resolved optical emission spectroscopy. *J. Appl. Spectrosc.* **2012**, *78*, 855–860. [CrossRef]
39. de Vero, J.; Lopez, R.A.; Garcia, W.O.; Sarmago, R.V. Post deposition heat treatment effects of ceramic superconducting films produced by infrared Nd:YAG pulsed laser deposition. In *Heat Treatment*; Czerwinski, F., Ed.; InTechOpen: Winchester, UK, 2012; pp. 197–205. ISBN 978-953-51-0768-2.

40. de Vero, J.C.; Hwang, I.; Shin, H.; Santiago, A.; Lee, D.; Chang, J.; Kim, J.; Sarmago, R.; Song, J.H. Growth and superconducting properties of $Bi_2Sr_2CaCu_2O_{8-\delta}$ thin films incorporated with iridate nanoparticles. *Phys. Status Solidi A* **2014**, *211*, 1787–1793. [CrossRef]
41. Nakamura, D.; Tanaka, T.; Ikebuchi, T.; Ueyama, T.; Higashihata, M.; Okada, T. Synthesis of Spherical ZnO Microcrystals by Laser Ablation in Air. *Electro Commun. Jpn.* **2016**, *99*, 58–63. [CrossRef]
42. Santos-Putungan, A.; Singidas, B.; Sarmago, R. Manipulation of low temperature grown ZnO rigid structures via Atomic Force Microscope. *HCTL Open Int. J. Technol. Innov. Res.* **2014**, *11*, 1–8.
43. Santos-Putungan, A.B.; Empizo, M.J.F.; Yamanoi, K.; Vargas, R.M.; Arita, R.; Minami, Y.; Shimizu, T.; Salvador, A.A.; Sarmago, R.V.; Sarukura, N. Intense and fast UV emitting ZnO microrods fabricated by low temperature aqueous chemoical growth method. *J. Lum.* **2016**, *169*, 216–219.
44. Chen, Z.; Cvelbar, U.; Mozetic, M.; He, J.; Sunkara, M. Long-range ordering of oxygen-vacancy planes in $Fe_2O_3$ nanowires and nanobelts. *Chem. Mater.* **2008**, *20*, 3224–3228. [CrossRef]
45. Jaeger, R.C. Thermal Oxidation of Silicon. In *Introduction to Microelectronic Fabrication*; Prentice Hall Inc.: New York, NY, USA, 2001; p. 30.
46. Arthur, J.R. Reaction between C and $O_2$. *Trans. Faraday Soc.* **1951**, *47*, 164–177. [CrossRef]
47. Jasmin, A.; Rillera, H.; Semblante, O.; Sarmago, R. Surface morphology, microstructure, raman characterization and magnetic ordering of oxidized Fe-sputtered films on silicon substrate. *AIP Conf. Proc.* **2012**, *1482*, 572–577.
48. Maslar, J.; Hurst, W.; Bowers, W.; Hendricks, J.; Aquino, M. In situ raman spectroscopic investigation of aqueous iron corrosion at elevated temperatures and pressures. *J. Electrochem. Soc.* **2000**, *147*, 2532–2542. [CrossRef]
49. Moon, J.; Sahajwalla, V. Kinetic model for the uniform conversion of self-reducing iron oxide carbon briquettes. *ISIJ Int.* **2003**, *43*, 1136–1142. [CrossRef]
50. Crank, J. *Mathematics of Diffusion*, 2nd ed.; Oxford Science Publications: Oxford, UK, 1975; p. 36.
51. Chen, M.; Yue, Y.; Jun, Y. Growth of metal and metal oxide nanowires driven by the stress-induced migration. *J. Appl. Phys.* **2012**, *11*, 104305. [CrossRef]
52. Yuan, L.; Wang, Y.; Cai, R.; Jiang, Q.; Wang, J.; Li, B.; Sharma, A.; Zhou, G. The origin of hematite nanowire growth during thermal oxidation of iron. *Mater. Eng. B* **2012**, *177*, 327–336. [CrossRef]
53. Kim, D.; Gosele, U.; Zacharias, M. Surface-diffusion induced growth of ZnO nanowires. *J. Cryst. Growth* **2009**, *311*, 3216–3219. [CrossRef]
54. Shih, P.-H.; Wu, S. Growth mechanism studies of ZnO nanowires: Experimental observations and short-circuit diffusion analysis. *Nanomaterials* **2017**, *7*, 188. [CrossRef]
55. Cutinho, J.; Chang, B.S.; Oyola-Reynoso, S.; Chen, J.; Akhter, S.S.; Tevis, I.; Bello, N.; Martin, A.; Foster, M.; Thuo, M. Automous thermal-oxidative composition inversion and texture tuning of liquid metal surfaces. *ACS Nano* **2018**, *12*, 4744–4753. [CrossRef] [PubMed]